Flexural wave propagation in canonical quasicrystalline-generated waveguides

Zhijiang Chen [a], Massimiliano Gei [b,*], Lorenzo Morini [c]

[a] *College of Aerospace Engineering, Chongqing University, Chongqing 400030, China*
[b] *Department of Engineering and Architecture, University of Trieste, via A. Valerio 6/1, 34127 Trieste, Italy*
[c] *Department of Mechanical, Chemical and Materials Engineering, University of Cagliari, via Marengo 9, 09123 Cagliari, Italy*

ARTICLE INFO

ABSTRACT

We investigate the propagation of harmonic flexural waves in periodic two-phase phononic multi-supported continuous beams whose elementary cells are designed according to the quasicrystalline standard Fibonacci substitution rule. The resulting dynamic frequency spectra are studied with the aid of a trace-map formalism which provides a geometrical interpretation of the recursive rule governing traces of the relevant transmission matrices: the traces of three consecutive elementary cells can be represented as a point on the surface defined by an invariant function of the square root of the circular frequency, and the recursivity implies the description of a discrete orbit on the surface. In analogy with the companion axial problem, we show that, for specific layouts of the elementary cell (the *canonical* configurations), the orbits are almost periodic. Likewise, for the same layouts, the stop-/pass-band diagrams along the frequency domain are almost periodic. Several periodic orbits exist and each corresponds to a self-similar portion of the dynamic spectra whose scaling law can be investigated by linearising the trace map in the neighbourhood of the orbit. The obtained results provide a new piece of theory to better understand the dynamic behaviour of two-phase flexural periodic waveguides whose elementary cell is obtained from quasicrystalline generation rules.

1. Introduction

Wave propagation in mechanical metamaterials and their applications in several fields of engineering have attracted much attention from the scientific community in the last twenty years. This was mainly due to the discovery of new phenomena for controlling waves, such as wave focussing (Yang et al., 2004; Tol et al., 2017), cloaking (Norris, 2008; Brun et al., 2009), negative refraction (Zhang and Liu, 2004; Morvan et al., 2010; Srivastava, 2016; Morini et al., 2019a) and topological edge modes (Wang et al., 2015; Ma et al., 2018; Rosa et al., 2019).

Recently, many researchers have focused on elastodynamics of composite beams constructed following a quasiperiodic pattern (Gei, 2010; Sorokin, 2019; Pal et al., 2019; Xia et al., 2020) (for recent developments on the dynamics of quasiperiodic media see, e.g. Chen et al., 2020; Beli et al., 2022; Davies and Craster, 2022; Bacigalupo et al., 2022; Davies et al., 2023). In particular, the non-standard dispersive properties of two-phase periodic structured rods whose unit cells are generated according to the Fibonacci substitution rule have been studied in detail (Gei, 2010; Morini and Gei, 2018; Morini et al., 2019b). This substitution rule belongs to the subset of quasicrystalline

one (Poddubny and Ivchenko, 2010; Zhang, 2017) and portions of Floquet-Bloch frequency spectra of its members display self-similar patterns which scale according to factors related to an invariant function, the Kohmoto's invariant (Kohmoto and Oono, 1984; Gei, 2010).

A step forward in the investigation was the determination of *canonical* elementary cells (Gei et al., 2020) that are constructed by following rational ratii between mechanical and geometrical properties of the phases. Frequency spectra of canonical configurations display periodic properties and symmetries so that the arrangement of pass and stop bands can be easily predicted. These features have found application not only in 1D waveguides (Gei et al., 2020; Morini et al., 2019b; Farhat et al., 2022), but also to predict the ranges of frequency for which shear horizontal waves in laminates are refracted with a negative index (Chen et al., 2022, 2023).

As an additional important feature, canonical layouts can take advantage of the properties of a discrete map connecting traces of three transmission matrices associated with elementary cells whose indices are consecutive (Kolar and Ali, 1989). This with the aim to reveal that said self-similarity can be linked to the periodic orbits described by the map on the invariant surface associated with Kohmoto's invariant (Gei

---

* Corresponding author.
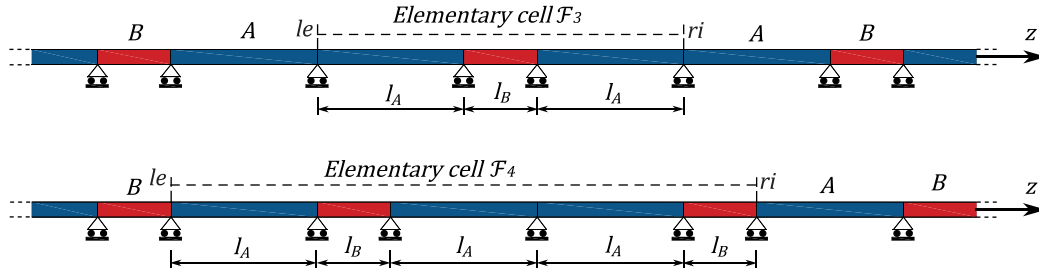*E-mail address:* massimiliano.gei@dia.units.it (M. Gei).

Fig. 1. Flexural waves in multi-supported beams generated by standard Fibonacci sequences $\mathcal{F}_3$ (top) and $\mathcal{F}_4$ (bottom). Symbols ri and le denote right and left-hand boundary of the cells, respectively.

et al., 2020). The scaling parameter governing the different self-similar ranges of the spectra can then be calculated, which could be used to predict, design and optimise the filtering properties of canonical quasicrystalline-generated structures.

In this paper, we generalise these concepts to investigate the dynamic properties of infinite periodic multi-supported Euler–Bernoulli beams based on elementary cells conceived by adopting a standard Fibonacci substitution rule. The beam is homogeneous with constant bending stiffness and density of mass per unit length so that the inner structure of the cells is provided by the position of supports and their relative distances. This problem is solved by building the transmission matrices of elementary cells and applying the Floquet-Bloch technique, yielding a set of eigenvalue problems in the circular frequency. Since the beam is multi-supported, there are two degrees of freedom and the transmission matrix is 2×2. Though the order of the system is the same, the dispersion relation of a multi-supported beam is not identical to that of the analogous axial wave problem (Gei et al., 2020). Indeed, in the current study the expressions of traces involve both periodic trigonometric and hyperbolic functions and the frequency enters naturally with its square root. This is in contrast with the axial wave problem, where traces depend only on sines and cosines whose arguments are proportional to the frequency.

Our main results are that canonical configurations can be also found for the bending problem and the corresponding dispersion spectra tend to be periodic and symmetric because the hyperbolic functions that appear in the dispersion relation can be approximated by periodic functions at moderately high frequencies. In the final part of the paper, we obtain analytical scaling factors governing the self-similarity properties of stop and pass bands so that the theory developed for the axial problem can be also profitably applied to multi-supported homogeneous beams guiding flexural waves.

2. Analysing of flexural wave propagation

We introduce a particular class of infinite two-phase periodic multi-supported beams whose elementary cells are generated by adopting the standard Fibonacci sequence $\mathcal{F}_i$ based on the recursion rule $\mathcal{F}_i = \mathcal{F}_{i-1}\mathcal{F}_{i-2}$.[1] The homogeneous basic constituents are A and B and the initial condition for the rule is $\mathcal{F}_0 = B$ and $\mathcal{F}_1 = A$ (see, e.g., Fig. 1).

Bending stiffness EI and mass density per unit length ρ are kept constant along the structure, therefore the distinction between the two elements A and B lies only on the distance l_X ($X \in \{A, B\}$) between supports. The total length of cell $\mathcal{F}_i$ is given by $L_i = n_i^{(A)}l_A + n_i^{(B)}l_B$, where $n_i^{(A)}$ and $n_i^{(B)}$ are the number of spans A and B included in the cell, respectively, and the total number of spans corresponds to the Fibonacci number $n_i = n_i^{(A)} + n_i^{(B)}$.

By assuming the co-ordinate z depicted in Fig. 1, the equation governing harmonic vibrations of the transverse displacement $v(z)$ for the Euler–Bernoulli beam is

$$EI\frac{d^4 v}{dz^4} - \rho\omega^2 v = 0. \tag{1}$$

Its solution can be sought in the form $v(z) = B\exp(\mathrm{i}kz)$ where B is constant and i is the imaginary unit. Eq. (1) yields the characteristic equation

$$(kr)^4 - D\omega^2 = 0, \tag{2}$$

where r is the radius of inertia of the cross section ($r^2 = I/\mathcal{A}$, where $\mathcal{A}$ is the beam cross-section area and I denotes its second-order moment) and $D = \rho r^4/EI$. Eq. (2) provides four solutions in k, namely

$$k_{1,2}(\omega) = \pm\frac{1}{r}\sqrt{\omega\sqrt{D}}, \quad k_{3,4}(\omega) = \pm\frac{1}{r}\sqrt{-\omega\sqrt{D}}, \tag{3}$$

where the first index in both expressions corresponds to the sign '+'.

We can now obtain the dispersion relation following the same procedure adopted in analysing the companion axial wave problem (Gei et al., 2020; Morini et al., 2019b; Farhat et al., 2022). As the beam is multi-supported, the state vector is determined by the rotation $\varphi(z)$ and its derivative $\varphi'(z)$ (alternatively, bending moment $M(z) = -EI\varphi'(z)$) at each supported point. This also means that the fourth-order differential system (1) has only two degrees of freedom under these constraints, as investigated by Gei (2010). The state vector on the right-hand side of cell $\mathcal{F}_i$ is then given by $V_{\mathcal{F}_i} = [\varphi_{\mathcal{F}_i}, \varphi'_{\mathcal{F}_i}]^T$ and is related to that on the left-hand side, say $V_0 = [\varphi_0, \varphi'_0]^T$, via the relationship

$$V_{\mathcal{F}_i} = M_i V_0, \tag{4}$$

where, M_i is the global transmission matrix for cell $\mathcal{F}_i$. The matrix is the result of the product

$$M_i = \prod_{p=1}^{n_i}[M_X]_p \quad (X \in \{A, B\}). \tag{5}$$

For this system, the transmission matrix $M_X(\omega)(X \in \{A, B\})$ associated with each constituent unit is

$$M_X = \begin{bmatrix} \dfrac{\psi_{bb}^X(\omega)}{\psi_{ab}^X(\omega)} & \psi_{ba}^X(\omega) - \dfrac{\psi_{bb}^X(\omega)\psi_{aa}^X(\omega)}{\psi_{ab}^X(\omega)} \\ \dfrac{1}{\psi_{ab}^X(\omega)} & -\dfrac{\psi_{aa}^X(\omega)}{\psi_{ab}^X(\omega)} \end{bmatrix}, \tag{6}$$

where

$$\psi_{aa}^X(\omega) = \frac{k_1(\omega)\cot(k_1(\omega)l_X) - k_3(\omega)\cot(k_3(\omega)l_X)}{k_3^2(\omega) - k_1^2(\omega)}, \quad \psi_{bb}^X(\omega) = -\psi_{aa}^X(\omega), \tag{7}$$

$$\psi_{ab}^X(\omega) = \frac{k_1(\omega)\csc(k_1(\omega)l_X) - k_3(\omega)\csc(k_3(\omega)l_X)}{k_3^2(\omega) - k_1^2(\omega)}, \quad \psi_{ba}^X(\omega) = -\psi_{ab}^X(\omega). \tag{8}$$

Functions $\psi_{aa}^X(\omega)$ and $\psi_{ab}^X(\omega)$ both take real values as k_3^2, $k_3\cot(k_3 l_X)$, $k_3\csc(k_3 l_X)$ are real and despite the fact that $k_3(\omega)$ is always an imaginary number. Further, matrix M_i possesses two relevant properties: (i) it is unimodular, i.e. $\det(M_i) = 1$; (ii) as a consequence of the recursion rule valid for the Fibonacci sequence, it can be generated through the recursive relationship $M_i = M_{i-2}M_{i-1}$ ($i \geq 2$). As a consequence, using

---

[1] The natural number i is the index of the element $\mathcal{F}_i$.

the Floquet-Bloch condition $V_{\mathcal{F}_i} = \exp(iKL_i)V_0$ in Eq. (4), the dispersion equation takes the form

$$|M_i - \exp(iKL_i)E| = 0, \tag{9}$$

where E is the identity matrix. Bloch wavenumber KL_i is expressed by the trace of matrix M_i

$$KL_i = \arccos\left(\frac{trM_i}{2}\right). \tag{10}$$

The solution to Eq. (10) provides the complete Floquet-Bloch spectrum and allows to obtain the mentioned stop-/pass-band pattern of the waveguides at varying index i. In particular, waves propagate when $|trM_i| < 2$ and KL_i is a real number, stop bands correspond to $|trM_i| > 2$ and KL_i is complex number associated with evanescent waves, whereas $|trM_i| = 2$ is the condition for standing waves.

3. Canonical configurations of multi-supported beams

This section is devoted to the investigation of properties of traces trM_i and how these features affect the dispersion diagram of flexural waves in multi-supported beams. A nonlinear recursive rule linking traces for three consecutive fundamental cells is introduced. Moreover, an invariant function defined by this maps that can be represented by a surface in a 3D space. At any frequency, the evolution of the traces corresponds to a discrete orbit on this surface (Kohmoto's surface). By means of this analysis, we introduce canonical configurations for these structures, leading to dynamics spectra that are close to be periodic and with some symmetries. The concept of canonical frequency is studied and is associated with periodic orbits on the Kohmoto's surface.

3.1. Nonlinear map and Kohmoto's invariant

General recursive relations for the traces of unimodular 2×2 transmission matrix of generalised Fibonacci chains have been derived in terms of Chebyshev polynomials of first and second kind (Kolar and Ali, 1989). According to the theory, three adjacent traces satisfy the recursive rule

$$x_{i+1} = x_{i-1}x_i - x_{i-2} \quad (i > 2), \tag{11}$$

where $x_i = trM_i$, with initial conditions

$$x_0 = 2\frac{\cosh\xi_B \sin\xi_B - \cos\xi_B \sinh\xi_B}{\sin\xi_B - \sinh\xi_B}, \quad x_1 = 2\frac{\cosh\xi_A \sin\xi_A - \cos\xi_A \sinh\xi_A}{\sin\xi_A - \sinh\xi_A},$$

$$x_2 = 2\frac{\cosh(\xi_A + \xi_B)\sin\xi_A \sin\xi_B + \cos(\xi_A + \xi_B)\sinh\xi_A \sinh\xi_B}{(\sin\xi_A - \sinh\xi_A)(\sin\xi_B - \sinh\xi_B)}$$

$$+ 2\frac{\sin\xi_B \sinh\xi_B + \sin\xi_A \sinh\xi_A - \sin(\xi_A + \xi_B)\sinh(\xi_A + \xi_B)}{(\sin\xi_A - \sinh\xi_A)(\sin\xi_B - \sinh\xi_B)}, \tag{12}$$

where normalised variables $\xi_X = k_1 l_X = \sqrt{\omega\sqrt{D}l_X}/r$ are introduced, similar to those adopted as coordinates on the representation based on the universal torus (Shmuel and Band, 2016; Morini et al., 2019b).

A new set of variables, namely

$$\tilde{x}_i = x_{i+2}, \quad \tilde{y}_i = x_{i+1}, \quad \tilde{z}_i = x_i, \tag{13}$$

can be defined singling out the triplet $R_i = (\tilde{x}_i, \tilde{y}_i, \tilde{z}_i)$ and its substitution into Eq. (12) leads to the following nonlinear map $\mathcal{T}$ which determines the evolution of the point R_i:

$$R_{i+1} = \mathcal{T}(R_i) = (\tilde{x}_i\tilde{y}_i - \tilde{z}_i, \tilde{x}_i, \tilde{y}_i). \tag{14}$$

The jacobian of map (14), namely

$$J = \frac{\partial(\tilde{x}_{i+1}, \tilde{y}_{i+1}, \tilde{z}_{i+1})}{\partial(\tilde{x}_i, \tilde{y}_i, \tilde{z}_i)} = \begin{bmatrix} \tilde{y}_i & \tilde{x}_i & -1 \\ 1 & 0 & 0 \\ 0 & 1 & 0 \end{bmatrix}, \tag{15}$$

can be evaluated, showing that $\det J = -1$. Through a little algebra we can also show that the following invariant quantity does exist (Morini and Gei, 2018; Gei et al., 2020)

$$I(\omega) = \tilde{x}_i^2 + \tilde{y}_i^2 + \tilde{z}_i^2 - \tilde{x}_i\tilde{y}_i\tilde{z}_i - 4. \tag{16}$$

This means that, at a determined circular frequency ω, the value $I(\omega)$ is independent of the order i of the sequence $\mathcal{F}_i$. In the three-dimensional space spanned by the cartesian coordinate system $O\tilde{x}\tilde{y}\tilde{z}$, Eq. (16) is the equation of a two-dimensional manifold, the Kohmoto's surface. Points R_i obtained by iterating map $\mathcal{T}$ belong to this surface for any given frequency ω. The set of points generated through the iteration defines a discrete orbit on the surface. Also, the position of R_i can reveal if, at a given frequency ω, structures represented by cells $\mathcal{F}_i$, $\mathcal{F}_{i+1}$, $\mathcal{F}_{i+2}$ are/are not in a pass band; in particular, the frequency is in a pass band for the three cells if $\{|x_i|, |x_{i+1}|, |x_{i+2}|\} < 2$; in a stop band if $\{|x_i|, |x_{i+1}|, |x_{i+2}|\} > 2$.

3.2. Periodic orbits on Kohmoto's surface and traces of transmission matrix

To ease the representation of orbits on Kohmoto's surface and pattern for traces of transmission matrix, the four plots in Fig. 2 refer to a prototype multi-supported beam whose geometry is such that $l_B/l_A = 5$ ($\xi_B = 5\xi_A$).

In Fig. 2(a), the Kohmoto's surface for the invariant $I = 0$ in the three-dimensional space $O\tilde{x}\tilde{y}\tilde{z}$ (Eq. (16)) is represented. Note that this is just an example as the invariant can take different values depending on frequency; however the case $I = 0$ is relevant. Some representative points are sketched, namely, the saddle points (six in total, three of them are visible, in black, the other three are hidden) and three points (in blue and green) that will be considered later while introducing the concept of periodic orbit.

In Figs. 2(b) (c) (d) the Kohmoto's surface is sketched in the subspace $O\tilde{y}\tilde{z}$, where the white squares in the centre of the three panels match the pass-band interval. Therefore, a point $\hat{R}_i(\omega) = (\tilde{y}, \tilde{z}) = (x_{i+1}, x_i)$ belonging to these squares means that that frequency ω for both $\mathcal{F}_i$ and $\mathcal{F}_{i+1}$ lies in a pass band.

The curved, continuous trajectories sketched in the same three plots have parametric equations $(x_2(\omega), x_1(\omega))$, $(x_3(\omega), x_2(\omega))$, $(x_4(\omega), x_3(\omega))$ in (b), (c) and (d), respectively. All of them start from different coordinates which corresponds always to $\xi_A = \pi$ (the reason for which the lines start at $\xi_A = \pi$ and not at $\xi_A = 0$ is explained in the next subsection); in particular, the red line covers the initial range $\xi_A \in [\pi, 3\pi/2]$, after which the green line follows for the next range, up to $\xi_A = 2\pi$. Then, the trajectories continue for increasing frequency $\xi_A \in [2\pi, 3\pi]$ with patterns that display a symmetry with those sketched for which, in each panel, at $\xi_A = 3\pi$ the relevant points are almost coincident with those at $\xi_A = \pi$.

Finally, differently from the axial wave problem, $\mathcal{F}_1$ has a stop band in the spectrum (note that the green line in (b) is fully in a stop band as $x_1 > 2$ in that range). In addition, two stop bands of the path for $\mathcal{F}_2$ are indicated. Parts (c) and (d) of the figure can be similarity interpreted. In particular, the complexity of the trend of the line increases at increasing index i of the sequence.

3.3. Existence of canonical configurations

There are three significant kinds of orbits which can be followed by points R_i as a consequence of the iteration map (14): (i) periodic orbits, (ii) non-periodic bounded orbits and (iii) escaping orbits. At any frequency, the type of orbit is uniquely determined by the initial three traces $R_0 = (\tilde{x}_0, \tilde{y}_0, \tilde{z}_0)$ whose coordinates are given by expressions (12).

The dynamic governing equation for Euler–Bernoulli beams is a fourth-order one whose integral involves *non-periodic* hyperbolic functions sinh and cosh in the traces (12). It differs from that of the companion problems of axial waves in rods and shear horizontal waves
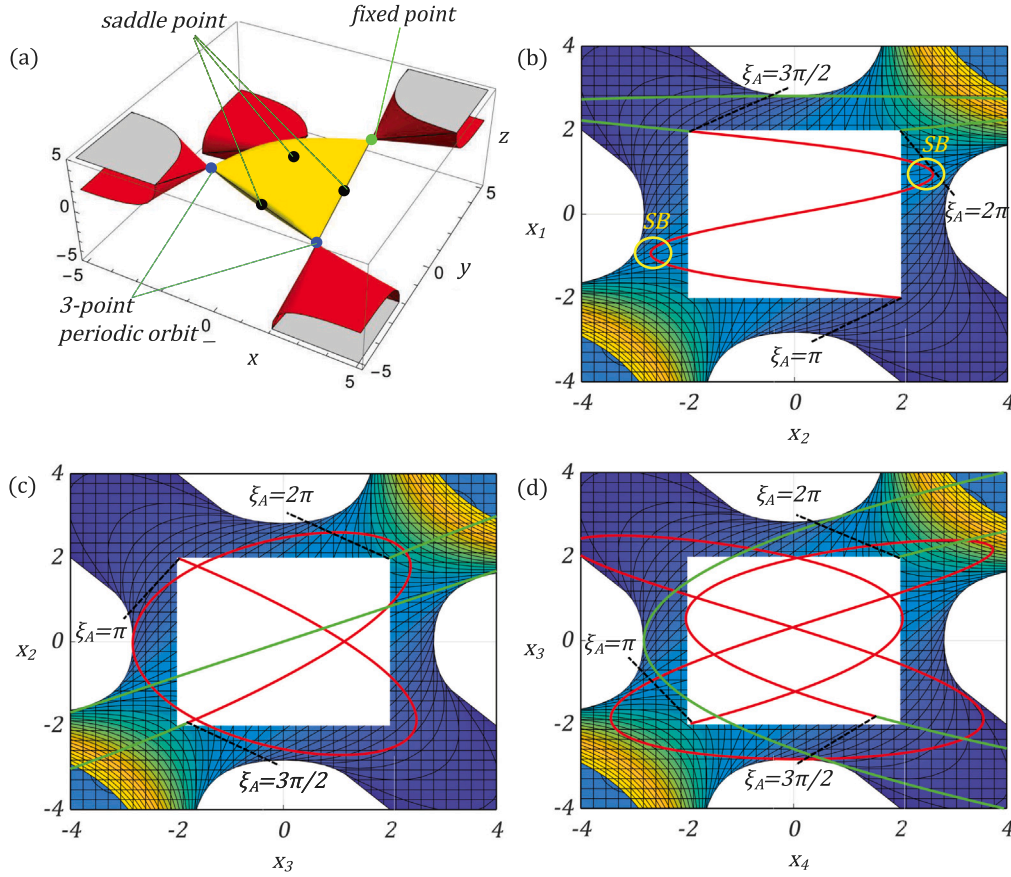
Fig. 2. (a) Kohmoto's surface for a multi-supported beam with $l_B/l_A = 5$. (a) Three-dimensional representation where three out of six saddle points are indicated with black colour, points of the three-point periodic orbit are blue; in green the so-called fixed point; (b), (c), (d) sketches in the plane $(\tilde{y}, \tilde{z})$, where the reported trajectories have parametric equations: (b) $(x_2(\omega), x_1(\omega))$; (c) $(x_3(\omega), x_2(\omega))$; (d) $(x_4(\omega), x_3(\omega))$. In all plots of (b), (c), (d) the red line is for dimensionless frequency $\xi_A \in [\pi, 3\pi/2]$, the green one is for $\xi_A \in [3\pi/2, 2\pi]$. In (b), two 'stop bands' (SB) are indicated for the function $x_2(\xi_A)$.
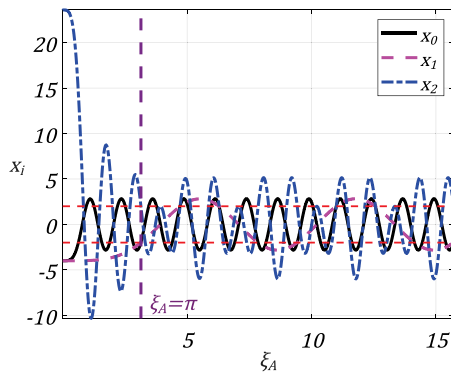

Fig. 3. Behaviour of functions x_0, x_1 and x_2 of the structure with $l_B/l_A = 5$ plotted against the dimensionless frequency ξ_A. Black, magenta and blue lines represent x_0, x_1 and x_2, respectively; red-dashed lines are for ± 2. The vertical, purple line marks $\xi_A = \pi$.

in laminates because, there, the involved functions in the solution are only periodic trigonometric ones. The first three traces of the structure with $l_B/l_A = 5$ are plotted against coordinate ξ_A in Fig. 3 to explain the reason for which a 'periodic' pattern can be recognised for $\xi_A > \pi$.

The limits for the three functions as $\omega \to 0$ are

$$\lim_{\omega \to 0} x_0 = \lim_{\omega \to 0} x_1 = -4; \quad \lim_{\omega \to 0} x_2 = 8 + 3\left(\frac{l_B}{l_A} + \frac{l_A}{l_B}\right). \tag{17}$$

The functions in Fig. 3 depart from the limits (17), start to oscillate, and beyond $\xi_A = \pi$ their behaviour becomes almost periodic; the reason is that, taking for instance x_0 and x_1 as references, the difference in a period π of the functions is given by

$$\frac{\cosh(\xi + 2\pi)\sin(\xi + 2\pi) - \cos(\xi + 2\pi)\sinh(\xi + 2\pi)}{\sin(\xi + 2\pi) - \sinh(\xi + 2\pi)} - \frac{\cosh\xi\sin\xi - \cos\xi\sinh\xi}{\sin\xi - \sinh\xi} =$$

$$\frac{2\sin\xi\sinh(\pi)(\cosh(\pi) - \cos\xi\cosh(\xi + \pi) + \sin\xi\sinh(\xi + \pi))}{(\sin\xi - \sinh\xi)(\sin\xi - \sinh(\xi + 2\pi))}, \tag{18}$$

that is an oscillating function tending to *zero* at increasing frequency and with relatively small values yet at $\xi = \pi$. Eq. (18) proves that the traces x_0 and x_1 of the transmission matrices of $\mathcal{F}_0$ and $\mathcal{F}_1$ for multi-supported beams are not periodic, but can be profitably approximated to periodic. This conclusion is valid for all traces despite the fact that the analogous of (18) for higher indices are much more complicated expressions.

Now, as the traces are 'almost' periodic, we can check if the theory of *canonical structures* developed by Gei et al. (2020) for axial wave propagation is also valid for flexural waves in multi-supported beams and is able to explain the scaling between parts of the frequency spectra at increasing index i.

In particular, considering the shape of the Kohmoto's surface (Fig. 2(a)), we focus on its saddle points denoted by P_k ($k = 1, \ldots, 6$), opposite in pairs, whose coordinates are $P_{2,5} = (\pm\alpha_1, 0, 0)$, $P_{3,6} = (0, \mp\alpha_2, 0)$, $P_{1,4} = (0, 0, \pm\alpha_3)$, where the top sign is associated with the lowest index and coefficients α_q ($q = 1, 2, 3$) depend on frequency and value of the invariant. In the axial wave problem, those points are such that $\mathcal{T}^6(P_k) = P_k$, $\forall k$, i.e. a 6-point periodic orbit exists connecting

Table 1
The characteristics of canonical multi-supported beams.

$C = 1 + 2j$	j even	j odd	j odd
$\omega_c(n)$	$\left(\frac{(5+4n)r\pi}{4D^{1/4}}\right)^2$, $n \in \mathbb{N}$	$\left(\frac{(5+4n)r\pi}{4D^{1/4}}\right)^2$, $n \in \mathbb{N}$	$\left(\frac{(7+4n)r\pi}{4D^{1/4}}\right)^2$, $n \in \mathbb{N}$
$(\tilde{x}_0, \tilde{y}_0, \tilde{z}_0)$	$\approx(\pm 2, 0, 0)$	$\approx(0, 0, \pm 2\sqrt{2})$	$\approx(0, \pm 2\sqrt{2}, 0)$

all the points. Therefore, the question naturally arises: which type of elementary cell can be represented by such a periodic orbit on the surface (16)? The answer is that, at some frequencies, one of the following three conditions must be satisfied (Gei et al., 2020):

$$(1) \ \tilde{y}_0 = \tilde{z}_0 = 0, \quad (2) \ \tilde{x}_0 = \tilde{z}_0 = 0, \quad (3) \ \tilde{x}_0 = \tilde{y}_0 = 0. \quad (19)$$

These requirements can be obtained only for a special set of configurations, called *canonical configurations*, at particular frequency values, the *canonical frequencies*. Conditions (19) imply that two out of the three traces (12) vanish. They lead to the following requirements in terms of lengths ratio (*canonical ratio*):

$$C = \frac{l_B}{l_A} = 1 + 2j \quad \text{or} \quad C = \frac{l_B}{l_A} = \frac{1}{1+2k} \quad (j, k \in \mathbb{N}). \quad (20)$$

These expressions are particular cases of *canonical configurations* for rods (Gei et al., 2020; Farhat et al., 2022) and laminates (Chen et al., 2022, 2023); they can be written in a more general form

$$C = \frac{l_B}{l_A} = \frac{1+2j}{1+2k} \quad (j, k \in \mathbb{N}). \quad (21)$$

In this paper, we only focus on cases where $k = 0$, which let $\xi_B \geq \pi$ when $\xi_A = \pi$ (as $C = \xi_B/\xi_A$). Other cases for $j = 0$ ($k \neq 0$) can be analysed in a similar fashion.

In the axial problem, conditions (19) can be satisfied exactly. In the current one, due to the presence of the hyperbolic functions, it is impossible to achieve a strict zero in the equations. However, we will see that the satisfaction of (19) will provide an almost exact theory that is very useful to interpret effectively the dispersion properties of quasicrystalline-generated multisupported flexural waveguides. Thus, the characteristics of *canonical multi-supported beams* (canonical ratio, frequency and values of the first three traces) are shown in Table 1. Moreover, for the problem currently investigated, the coordinates appearing in the saddle point are $\alpha_1 \approx 2$, $\alpha_2 \approx \alpha_3 \approx 2\sqrt{2}$, as shown in Table 1. The three cases presented in the table are studied in detail in the next subsections.

3.3.1. Index j is even

When index j is *even*, by substituting $\omega_c(0) = \left(\frac{5r\pi}{4D^{1/4}}\right)^2$ into traces (12), the variables ξ_A and ξ_B assume the values $\xi_A = 5\pi/4$ and $\xi_B = 5(1+2j)\pi/4$, whereas x_0, x_1 and x_2 take the form:

$$x_0 = 2\sqrt{2}\frac{\cosh(5(1+2j)\pi/4) - \sinh(5(1+2j)\pi/4)}{\sqrt{2} + 2\sinh(5(1+2j)\pi/4)}, \quad \text{with } j = 4m, \ m \in \mathbb{N},$$

$$x_0 = 2\sqrt{2}\frac{\cosh(5(1+2j)\pi/4) - \sinh(5(1+2j)\pi/4)}{\sqrt{2} - 2\sinh(5(1+2j)\pi/4)}, \quad \text{with } j = 4m+2, \ m \in \mathbb{N},$$

$$x_1 = 2\sqrt{2}\frac{\cosh(5\pi/4) - \sinh(5\pi/4)}{\sqrt{2} + 2\sinh(5\pi/4)},$$

$$x_2 = 2\frac{\cosh(\frac{5(1+j)\pi}{2}) - 2\sinh(\frac{5(1+j)\pi}{2}) - \sqrt{2}(\sinh(\frac{5\pi}{4}) + \sinh(\frac{5(1+2j)\pi}{4}))}{(1 + \sqrt{2}\sinh(\frac{5\pi}{4}))(1 + \sqrt{2}\sinh(\frac{5(1+2j)\pi}{4}))},$$

with $j = 4m$, $m \in \mathbb{N}$,

$$x_2 = 2\frac{\cosh(\frac{5(1+j)\pi}{2}) - 2\sinh(\frac{5(1+j)\pi}{2}) - \sqrt{2}(\sinh(\frac{5\pi}{4}) - \sinh(\frac{5(1+2j)\pi}{4}))}{(1 + \sqrt{2}\sinh(\frac{5\pi}{4}))(1 - \sqrt{2}\sinh(\frac{5(1+2j)\pi}{4}))},$$

with $j = 4m+2$, $m \in \mathbb{N}$. $\quad (22)$

From the expressions above, it can be deduced that at frequency $\omega_c(0)$, $x_0 \approx x_1 \approx 0$ and x_2 can be approximated to ± 2 depending on whether parameter j is $4m$ or $4m + 2$. Then, the representative point on the Kohmoto's surface at frequency $\omega_c(0)$ is in the neighbourhood of $(\pm 2, 0, 0)$ (saddle points P_2 and P_5); in the companion axial problem, this occurrence corresponds to *canonical configurations of family one*. With a similar procedure, the case $\omega_c(1)$ can be studied, giving $\xi_A = 9\pi/4$ and $\xi_B = 9(1+2j)\pi/4$; the point on the surface is again in the neighbourhood of $(\pm 2, 0, 0)$. Therefore, as a conclusion, the canonical frequencies for j *even* are given by $\omega_c(n) = \left(\frac{(5+4n)r\pi}{4D^{1/4}}\right)^2$ ($n \in \mathbb{N}$[2]).

3.3.2. Index j is odd-1

As a second case, when j is *odd*, by substituting $\omega_c(0) = \left(\frac{5r\pi}{4D^{1/4}}\right)^2$ into traces (12), it turns out that $\xi_A = 5\pi/4$ and $\xi_B = 5(1+2j)\pi/4$, and the functions x_0, x_1, x_2 become

$$x_0 = 2\sqrt{2}\frac{\cosh(5(1+2j)\pi/4) + \sinh(5(1+2j)\pi/4)}{\sqrt{2} + 2\sinh(5(1+2j)\pi/4)}, \quad \text{with } j = 4m+1, \ m \in \mathbb{N},$$

$$x_0 = 2\sqrt{2}\frac{\cosh(5(1+2j)\pi/4) + \sinh(5(1+2j)\pi/4)}{\sqrt{2} - 2\sinh(5(1+2j)\pi/4)}, \quad \text{with } j = 4m+3, \ m \in \mathbb{N},$$

$$x_1 = 2\sqrt{2}\frac{\cosh(5\pi/4) - \sinh(5\pi/4)}{\sqrt{2} + 2\sinh(5\pi/4)},$$

$$x_2 = 2\frac{\cosh(\frac{5j\pi}{2}) - \sqrt{2}(\sinh(\frac{5\pi}{4}) + \sinh(\frac{5(1+2j)\pi}{4}))}{(1 + \sqrt{2}\sinh(\frac{5\pi}{4}))(1 + \sqrt{2}\sinh(\frac{5(1+2j)\pi}{4}))}, \quad \text{with } j = 4m+1, \ m \in \mathbb{N},$$

$$x_2 = 2\frac{\cosh(\frac{5j\pi}{2}) + \sqrt{2}(\sinh(\frac{5\pi}{4}) - \sinh(\frac{5(1+2j)\pi}{4}))}{(1 + \sqrt{2}\sinh(\frac{5\pi}{4}))(1 - \sqrt{2}\sinh(\frac{5(1+2j)\pi}{4}))}, \quad \text{with } j = 4m+3, \ m \in \mathbb{N}.$$

$$(23)$$

This time, $x_1 \approx x_2 \approx 0$ and $x_0 \approx \pm 2\sqrt{2}$, and the representative point on Kohmoto's surface is close to $(0, 0, \pm 2\sqrt{2})$ (P_1 and P_4; *canonical configuration of family three* in the axial problem). The results for $\omega_c(1)$, for which $\xi_A = 9\pi/4$ and $\xi_B = 9(1+2j)\pi/4$, can be obtained by following a similar procedure, leading again to canonical frequencies $\omega_c(n) = \left(\frac{(5+4n)r\pi}{4D^{1/4}}\right)^2$ ($n \in \mathbb{N}$).

3.3.3. Index j is odd-2

Furthermore, again for index j odd, the substitution of $\omega_c(0) = \left(\frac{7r\pi}{4D^{1/4}}\right)^2$ into traces (12) results in $\xi_A = 7\pi/4$ and $\xi_B = 7(1+2j)\pi/4$; the first three traces become

$$x_0 = 2\sqrt{2}\frac{\cosh(7(1+2j)\pi/4) - \sinh(7(1+2j)\pi/4)}{\sqrt{2} + 2\sinh(7(1+2j)\pi/4)}, \quad \text{with } j = 4m+1, \ m \in \mathbb{N},$$

$$x_0 = 2\sqrt{2}\frac{\cosh(7(1+2j)\pi/4) - \sinh(7(1+2j)\pi/4)}{\sqrt{2} - 2\sinh(7(1+2j)\pi/4)}, \quad \text{with } j = 4m+3, \ m \in \mathbb{N},$$

$$x_1 = 2\sqrt{2}\frac{\cosh(7\pi/4) + \sinh(7\pi/4)}{\sqrt{2} + 2\sinh(7\pi/4)},$$

$$x_2 = 2\frac{\cosh(\frac{7j\pi}{2}) - \sqrt{2}(\sinh(\frac{7\pi}{4}) + \sinh(\frac{7(1+2j)\pi}{4}))}{(1 + \sqrt{2}\sinh(\frac{7\pi}{4}))(1 + \sqrt{2}\sinh(\frac{7(1+2j)\pi}{4}))}, \quad \text{with } j = 4m+1, \ m \in \mathbb{N},$$

---

[2] To give an example of how the points of the orbits are in the neighbourhoods of saddle points, consider the case $j = 2$ ($C = 3$) reported in Fig. 4; at $\omega_c(0)$ ($\xi_A = 5\pi/4$), the representative point has coordinates $(2.0007, 0.0011, 0)$, very close to P_2, whereas after a period of six iterations, the point is now $(2.0008, 0.0139, -0.0086)$, again close to P_2. For $\omega_c(1)$ ($\xi_A = 9\pi/4$), the mismatch in the values of coordinates w.r.t. those of the saddle point is in the order of 10^{-6}.
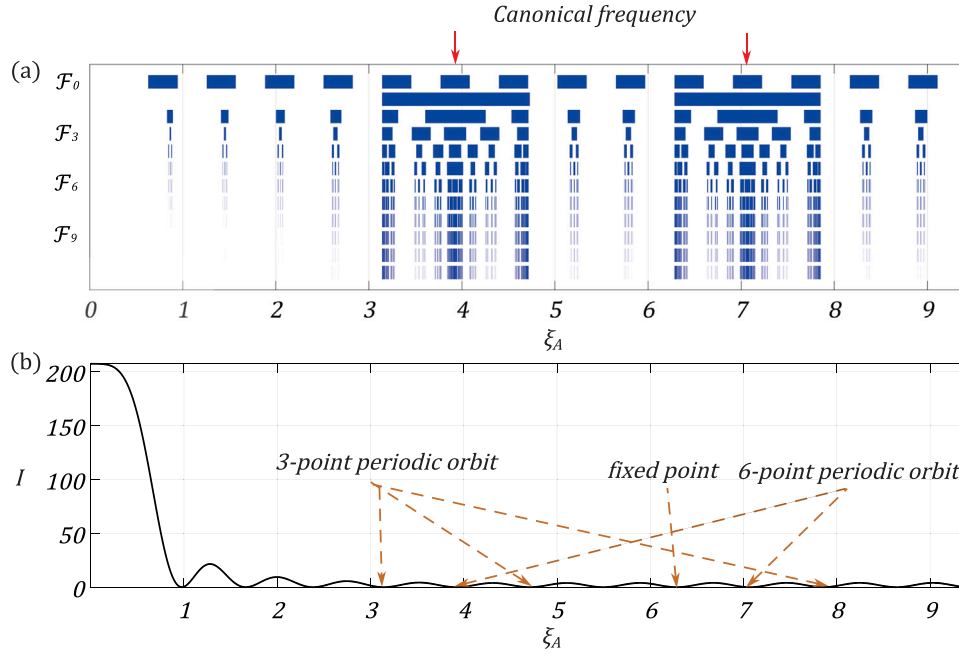
Fig. 4. Canonical multi-supported beam with $C = 5$. (a) stop-/pass-band layout in the same interval for sequences $\mathcal{F}_0$ to $\mathcal{F}_{11}$; (b) sketch of the invariant $I(\omega)$: the frequencies at which periodic orbits occur are indicated.

$$x_2 = 2\frac{\cosh(\frac{7j\pi}{2}) + \sqrt{2}(\sinh(\frac{7\pi}{4}) - \sinh(\frac{7(1+2j)\pi}{4}))}{(1 + \sqrt{2}\sinh(\frac{7\pi}{4}))(1 - \sqrt{2}\sinh(\frac{7(1+2j)\pi}{4}))}, \quad \text{with } j = 4m+3, \ m \in \mathbb{N},$$

(24)

from which it can be deduced that $x_0 \approx x_2 \approx 0$ and $x_1 \approx \pm2\sqrt{2}$. This point is in the vicinity of $(0, \pm2\sqrt{2}, 0)$ (P_3 and P_6; *canonical configuration of family two* in the axial problem). Following an analogous process, the results from case $\omega_c(1)$, for which $\xi_A = 11\pi/4$ ($n = 1$) and $\xi_B = 11(1 + 2j)\pi/4$, can be obtained. Hence, under these conditions, the canonical frequencies are given by $\omega_c(n) = \left(\frac{(7+4n)r\pi}{4D^{1/4}}\right)^2$ ($n \in \mathbb{N}$).

3.4. Stop-/pass-band layouts for canonical configurations

To illustrate the features of dispersion diagrams of *canonical multi-supported beams*, the diagram of stop and pass bands for two examples, i.e. $C = 5$ ($j = 2$) and $C = 3$ ($j = 1$), are displayed in Figs. 4 and 5, respectively.

In Fig. 4(a), the layout is sketched for all cells of the range $\mathcal{F}_0$ to $\mathcal{F}_{11}$ in which the blue segment denotes a pass band whereas a blank indicates a stop band. It can be noticed that beyond $\xi_A = \pi$ the pattern is almost *symmetric* and *periodic*. The canonical frequencies, indicated with red arrows in both Figs. 4 and 5, set the axis of symmetry of the pattern and indicate the occurrence of 6-point periodic orbits on the Kohmoto's surface. In the range displayed in Figs. 4(a) and 5(a), there are two and four canonical frequencies, respectively, that satisfy our theoretical analysis. In addition, the value of the invariant, as shown in Figs. 4(b) and 5(b), decreases from a relatively large value reached at the beginning of the domain and becomes almost periodic for $\xi_A > \pi$, as stated earlier in the section.

In addition to that singled out by the saddle points, a variety of periodic orbits on the invariant surface are present, located at frequencies $\hat{\omega}$ for which $I(\hat{\omega}) = 0$. By considering now the canonical ratio $C = 1+2j$ [Eq. (20)], when $\xi_A = \pi$, and therefore $\xi_B = (1 + 2j)\pi$, the first three traces become:

$$x_0 = -2, \ x_1 = -2, \ x_2 = 2,$$

(25)

that are the coordinates of a point Q on Kohmoto's surface that is part of a 3-point periodic orbit, i.e. $\mathcal{T}^3(Q) = Q$ (see Fig. 2(a); the other two points of the orbit have coordinates: $x_0 = 2$, $x_1 = -2$, $x_2 = -2$, and $x_0 = -2$, $x_1 = 2$, $x_2 = -2$).

When $\xi_A = 3\pi/2$, then $\xi_B = 3(1+2j)\pi/2$, the three initial traces take the values

$$x_0 = 2\frac{\cosh(3(1 + 2j)\pi/2)}{1 + \sinh(3(1 + 2j)\pi/2)}, \quad \text{with } j \text{ even, or}$$

$$x_0 = 2\frac{\cosh(3(1 + 2j)\pi/2)}{1 - \sinh(3(1 + 2j)\pi/2)}, \quad \text{with } j \text{ odd,}$$

$$x_1 = 2\frac{\cosh(3\pi/2)}{1 + \sinh(3\pi/2)},$$

$$x_2 = 2\frac{(\cosh(3j\pi/2) - \sinh(3(1 + 2j)\pi/2))^2}{(1 + \sinh(3\pi/2))(1 + \sinh(3(1 + 2j)\pi/2))}, \quad \text{with } j \text{ even,}$$

$$x_2 = -2\frac{(\sinh(3j\pi/2) - \cosh(3(1 + 2j)\pi/2))^2}{(1 + \sinh(3\pi/2))(-1 + \sinh(3(1 + 2j)\pi/2))}, \quad \text{with } j \text{ odd,} \quad (26)$$

from which it can be observed that x_0 and x_2 approximate to ±2 (the sign depends whether index j is *even* or *odd*) whereas $x_1 \approx 2$. Thus, a point on Kohmoto's surface with these initial three traces is in the neighbourhood of one of the 3-point periodic orbit presented earlier. The points of the orbit get closer and closer to the periodic one at an increase of index j.

Analogously, when $\xi_A = 2\pi$, and then $\xi_B = 2(1 + 2j)\pi$, the three traces are equal, i.e.

$$x_0 = x_1 = x_2 = 2,$$

(27)

a condition associated with a *fixed point* on the Kohmoto's surface (see Fig. 2(a); the point is transformed in itself by the map $\mathcal{T}$).

As an additional remark, the analysis of the traces reveal that, in the variable ξ_A, the overall period is $\Xi_p = 2\pi$ (the analysis of the period from Figs. 4(a) and 5(a) could be misleading because the stop-/pass-band pattern depends on the absolute values of traces), so that in terms of square root of the circular frequency the period $\sqrt{\Omega_p}$ is equal to $\sqrt{\Omega_p} = 2\pi r/(l_A D^{1/4})$.
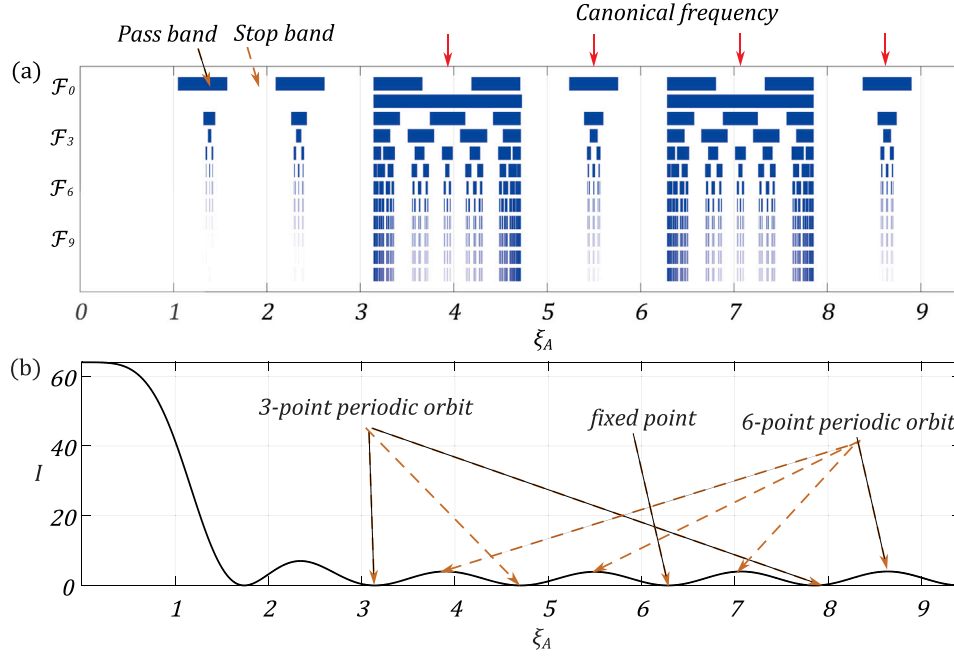
Fig. 5. Canonical multi-supported beam with $C = 3$. (a) stop-/pass-band layout in the same interval for sequences $\mathcal{F}_0$ to $\mathcal{F}_{11}$; (b) sketch of the invariant $I(\omega)$: the frequencies at which periodic point orbits occur are indicated.

Finally, a comment is needed regarding sensitivity to perturbations of geometrical parameters of the stop-/pass-band structure just described. On the one hand, we have altered by $\pm 0.01\%$ the value of l_B in ratio (20) for $C = 3$ (Fig. 5) and observed that the relative maximum change in the width of bands across the first canonical frequency ($\xi_A = 5\pi/4$) is $\approx 0.1\%$ for cell $\mathcal{F}_4$. On the other hand, a perturbation of $\pm 1\%$ of the same parameter resulted in a maximum change of $\approx 1\%$ of the band width for cell $\mathcal{F}_3$. Therefore, it is not possible to reach any definitive conclusion regarding sensitivity to perturbations of the stop-/pass-band diagram, but any specific case should be studied in detail.

4. Scaling and self-similarity of the dimensionless frequency spectra of canonical beams

In this section, analytical scaling factors which govern the self-similar pattern of stop-/pass-band layouts and traces of the transmission matrix of the canonical multi-supported beam are obtained through the linearisation of the map (14) about the associated periodic orbits.

4.1. Linearisation of the trace map about periodic points

Consider a point P_j as one of a p-periodic orbit. Let us assume, for a 'small' perturbation $\delta\sqrt{\omega}$, that $\bar{R}_i = R_i(\sqrt{\omega} + \delta\sqrt{\omega})$, where $R_i(\sqrt{\omega}) = P_j$. Then $\bar{R}_i$ is in the neighbourhood of the point P_j and the modulus of the vector $\delta\mathbf{r}_i(\delta\sqrt{\omega}) = \bar{R}_i - P_j$ is small with respect to the value of the non-vanishing coordinate of P_j. On the one hand, by applying p times the transformation $\mathcal{T}$, the exact position of $\bar{R}_{i+p} = \mathcal{T}^p(\bar{R}_i)$ can be obtained. On the other, due to the smallness of vector $|\delta\mathbf{r}_i|$, a linearisation of the nonlinear map can be performed such that the position of point $\bar{R}_{i+p}$ can be approximated by $P_j + \delta\hat{\mathbf{r}}_{i+p}$, where

$$\delta\hat{\mathbf{r}}_{i+p} = \bar{\mathbf{A}}_p \delta\mathbf{r}_i. \tag{28}$$

The linear operator $\bar{\mathbf{A}}_p$ depends on the orbit and the Jacobian (15), and is given by

$$\bar{\mathbf{A}}_p = \mathbf{J}(P_{j+p-1})\dots\mathbf{J}(P_j).$$

The 3×3 matrix $\bar{\mathbf{A}}_p$ whose determinants are ± 1 depending on whether p is even or odd as $\det\mathbf{J} = -1$. One eigenvalue of $\bar{\mathbf{A}}_p$ is $\kappa^0 = 1$, corresponding to the eigenvector $\boldsymbol{\psi}^0$, whereas the other two eigenvalues, κ^+ and κ^-, are reciprocal, i.e. $\kappa^+ = 1/\kappa^-$ (the associated eigenvector are $\boldsymbol{\psi}^\pm$). Thus, $\delta\mathbf{r}_i$ can be expressed as a linear combination of the three eigenvectors $\boldsymbol{\psi}^0$, $\boldsymbol{\psi}^+$ and $\boldsymbol{\psi}^-$ through coefficients C^+, C^- and C^0, respectively:

$$\delta\mathbf{r}_i = C^+\boldsymbol{\psi}^+ + C^-\boldsymbol{\psi}^- + C^0\boldsymbol{\psi}^0. \tag{29}$$

Therefore, by applying Eq. (28), it turns out that $\delta\hat{\mathbf{r}}_{i+p} = \bar{\mathbf{A}}_p\delta\mathbf{r}_i = C^+\kappa^+\boldsymbol{\psi}^+ + C^-\kappa^-\boldsymbol{\psi}^- + C^0\kappa^0\boldsymbol{\psi}^0$. One of the properties of the eigenvalues is that κ^+ tend to be dominant w.r.t. the other two, then the following approximation holds:

$$\delta\hat{\mathbf{r}}_{i+p} \approx C^+\kappa^+\boldsymbol{\psi}^+ \approx (\kappa^+)\delta\mathbf{r}_i. \tag{30}$$

It is worth noticing that, by inspection, the eigenvalues $\kappa^\pm$ for 3- and 6-periodic orbits are

$$\kappa^\pm(\omega) = \frac{1}{4}(\sqrt{4 + (4 + I(\omega))^2} \pm (4 + I(\omega)))^2. \tag{31}$$

Note also that if we are analysing a saddle point, eigenvector $\boldsymbol{\psi}^0$ is orthogonal to the tangent plane at P_j whereas the other two eigenvectors span the tangent plane. Therefore, vector $C^+\kappa^+\boldsymbol{\psi}^+$ belongs to the tangent plane itself. However, for both 3-point periodic orbit and fixed point, vector $C^+\kappa^+\boldsymbol{\psi}^+$ does not belong to the tangent plane itself, however the validity of the approximation (30) still holds (Gei et al., 2020).

4.2. Scaling of the dimensionless frequency spectra

Examples of the interpretation of the linearisation of the trace map as a method to explain scaling of the frequency spectra of canonical multi-supported beam are reported in Figs. 6–8, which analyse self-similar portions of the stop-/pass-band layouts at canonical frequencies displayed in Fig. 5 (in Figs. 6, 7) and 3-point periodic orbit and canonical frequency displayed in Fig. 4 (in Fig. 8).

Consider Figs. 6(a) and 7(a) where the traces in the vicinity of the canonical frequency $\xi_A = 9\pi/4$ (at which a 6-point periodic orbit
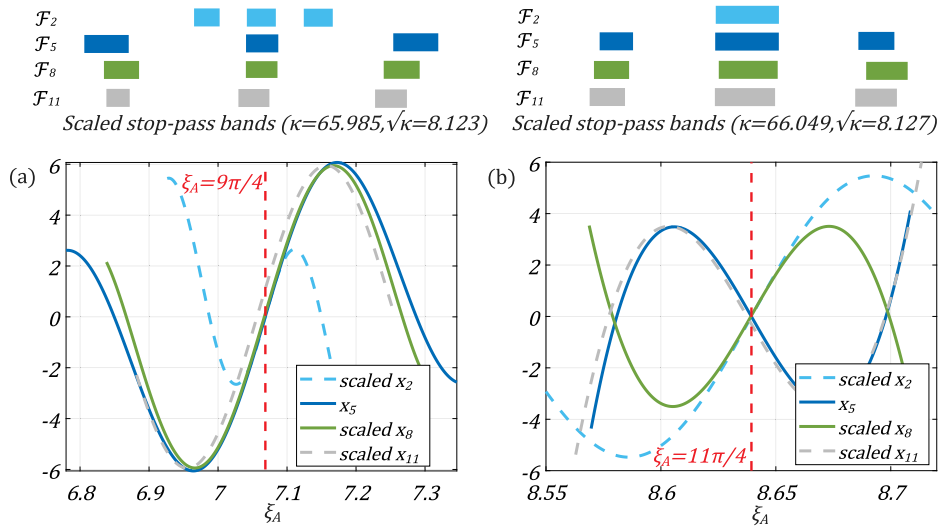
Fig. 6. Canonical multi-supported beam with $C = 3$ (see Fig. 5). Plot of traces $x_2(\sqrt{\omega}/\sqrt{\kappa})$, $x_5(\sqrt{\omega})$ (not scaled), $x_8(\sqrt{\omega}\sqrt{\kappa})$ and $x_{11}(\sqrt{\omega}\kappa)$ in the neighbourhood of canonical frequencies (a) $\xi_A = 9\pi/4$ ($\kappa = 65.985$) and (b) $\xi_A = 11\pi/4$ ($\kappa = 66.049$) where 6-point periodic orbits occur.
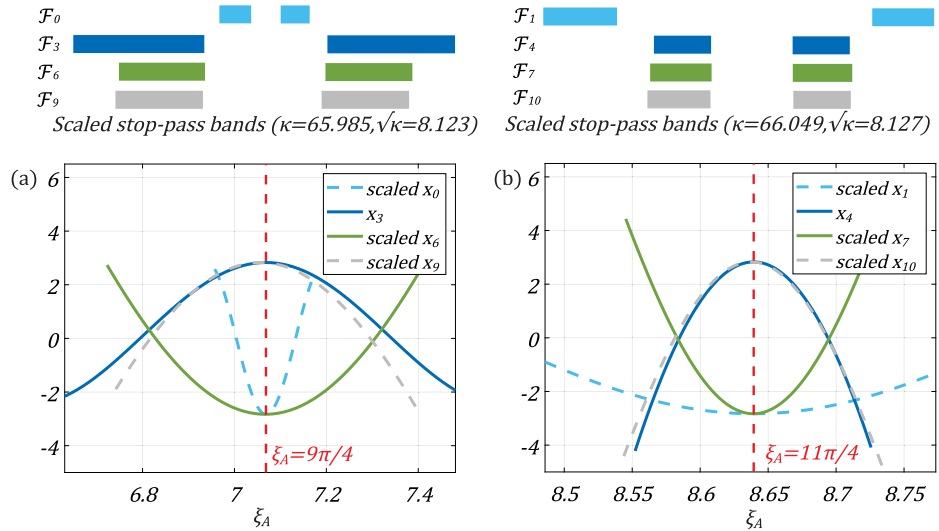

Fig. 7. Canonical multi-supported beam with $C = 3$ (see Fig. 5). (a) Plot of traces $x_0(\sqrt{\omega}/\sqrt{\kappa})$, $x_3(\sqrt{\omega})$ (not scaled), $x_6(\sqrt{\omega}\sqrt{\kappa})$ and $x_9(\sqrt{\omega}\kappa)$ in the neighbourhood of canonical frequency $\xi_A = 9\pi/4$ ($\kappa = 65.985$) and (b) $x_1(\sqrt{\omega}/\sqrt{\kappa})$, $x_4(\sqrt{\omega})$ (not scaled), $x_7(\sqrt{\omega}\sqrt{\kappa})$ and $x_{10}(\sqrt{\omega}\kappa)$ in the neighbourhood of canonical frequency $\xi_A = 11\pi/4$ ($\kappa = 66.049$) where 6-point periodic orbits occur.

occurs) are plotted and let us focus on functions x_5 (in the former figure) and x_3 (in the latter figure) that are not scaled; from their values, it can be inferred that the point that they represent on the surface is $R_3 = (0, 0, 2\sqrt{2})$ that coincides with saddle point P_1.

To the first order, vector $\delta\mathbf{r}_3(\delta\sqrt{\omega}) = \bar{R}_3(\sqrt{\omega} + \delta\sqrt{\omega}) - P_1(\sqrt{\omega})$ can be written as:

$$\delta\mathbf{r}_3(\delta\sqrt{\omega}) = \gamma\delta\sqrt{\omega}, \tag{32}$$

where $\gamma = \text{grad}_{\sqrt{\omega}}\delta\mathbf{r}_3$. Approximations (32) lies in the tangent plane spanned by coordinates x_4 and x_5. Therefore, we can say that, in the neighbourhood of $\xi_A = 9\pi/4$, $x_4 \approx \gamma_4\delta\sqrt{\omega}$ and $x_5 \approx \gamma_5\delta\sqrt{\omega}$, where γ_4, γ_5 are the projections of vector γ onto the axes x_4 and x_5, respectively.

With the completion of the cycle of six applications of the trace map, $x_{11} \approx \kappa^+\gamma_5\delta\sqrt{\omega}$ (henceforth, κ^+ will be substituted with κ for simplicity). This result is what is reported in Fig. 6(a), where the function x_{11} is scaled in the same domain of x_5 with the factor $\kappa = 65.985$, calculated, in turn, through Eq. (31). The match between the two functions, scaled accordingly, is very good. As shown in the plot, the scaling between x_2 and x_8 is set by the same factor and their match

is almost perfect about ξ_A. Similar considerations can be put forward for part (b) of the same figure that is centred on dimensionless canonical frequency $\xi_A = 11\pi/4$.

It is evident that about the canonical frequencies, the introduced linear approximation of traces explains quantitatively very well their behaviour. Consequently, there, the extent of pass bands centred at the canonical frequency at increasing index i can be predicted with good accuracy within the limit of the linearisation presented above, as shown at the top of Fig. 6.

An extension of the same line of reasoning leads to the conclusion that also after three applications of the trace map (then at half of the whole cycle) the scaling is valid, but governed by $\sqrt{\kappa}$. This is confirmed by all plots in Fig. 6(a) where functions x_2, x_5, x_8, x_{11} are displayed.

Due to the fact that traces appearing in Fig. 6 are null at the canonical frequency, the scaling studied in said figure is pertinent to pass bands. That for stop bands at the same frequency is represented in Fig. 7 where traces whose absolute values are always larger than 2 for $\xi_A = 9\pi/4$ and $\xi_A = 11\pi/4$ are sketched. In particular, let us focus on Fig. 7(a) in which x_3 is displayed in its natural domain whereas the

others (i.e. x_0, x_6, x_9) are scaled. We show now that, despite the fact that the functions are not linear, the scaling factor is still κ.

On the one hand, we have already shown that at $\xi_A = 9\pi/4$, x_4 and x_5 are linear, i.e. $x_4 \approx \gamma_4 \delta\sqrt{\omega}$ and $x_5 \approx \gamma_5 \delta\sqrt{\omega}$. On the other, at the lowest order, x_3 can be approximated with a quadratic function, namely $x_3 \approx 2\sqrt{2} - \zeta_3(\delta\sqrt{\omega})^2$, whereas the Taylor expansion of (16) provides an approximation of the invariant to the second order, i.e.

$$\delta I \approx \hat{I}\left(\frac{9\pi}{4}\right) - \frac{1}{2}\left[\hat{I}'\left(\frac{9\pi}{4}\right)\right]^2 (l_A - l_B)^2 \frac{D^{1/2}}{r^2}(\delta\sqrt{\omega})^2,$$

where $\hat{I}(\xi_A) = I(\omega)$. The use of the above approximations still in (16) yields, to the leading (second) order,

$$-\frac{1}{2}\left[\hat{I}'\left(\frac{9\pi}{4}\right)\right]^2 (l_A - l_B)^2 \frac{D^{1/2}}{r^2}(\delta\sqrt{\omega})^2$$
$$= (\gamma_5 \delta\sqrt{\omega})^2 + (\gamma_4 \delta\sqrt{\omega})^2 - 4\sqrt{2}\zeta_3(\delta\sqrt{\omega})^2 + 2\sqrt{2}\gamma_4\gamma_5(\delta\sqrt{\omega})^2, \quad (33)$$

from which

$$4\sqrt{2}\zeta_3 = \gamma_5^2 + \gamma_4^2 - 2\sqrt{2}\gamma_4\gamma_5 + \frac{1}{2}\left[\hat{I}'\left(\frac{9\pi}{4}\right)\right]^2 (l_A - l_B)^2 \frac{D^{1/2}}{r^2}. \quad (34)$$

Let us turn our attention now to the same saddle point (i.e. P_1, see the comment before Eq. (32)), but evaluated after a cycle of six applications of the trace map, i.e. $R_9|_{\xi_A=9\pi/4} \approx (0, 0, 2\sqrt{2})$. By repeating the same argument, we can write

$$x_{11} \approx \gamma_{11}\overline{\delta\sqrt{\omega}}, \quad x_{10} \approx \gamma_{10}\overline{\delta\sqrt{\omega}}, \quad x_9 \approx 2\sqrt{2} - \zeta_9(\overline{\delta\sqrt{\omega}})^2, \quad (35)$$

where, from the analysis performed on the functions in Fig. 6,

$$\gamma_{11} \approx \kappa\gamma_5, \quad \gamma_{10} \approx \kappa\gamma_4, \quad (36)$$

and the overbar has been added to the perturbation because we need to consider a scaled domain. Our goal is to find the connection between ζ_3 and ζ_9 through the factor κ. In particular, note that in analogy to the case illustrated in Fig. 6(a), x_{11} matches x_5 if $\overline{\delta\sqrt{\omega}} = \delta\sqrt{\omega}/\kappa$. Therefore, we can again consider Eq. (33) and substitute the terms of the r.h.s. with those expressed as a function of $\overline{\delta\sqrt{\omega}}$,

$$-\frac{1}{2}\left[\hat{I}'\left(\frac{9\pi}{4}\right)\right]^2 (l_A - l_B)^2 \frac{D^{1/2}}{r^2}(\delta\sqrt{\omega})^2$$
$$= (\gamma_{11}\overline{\delta\sqrt{\omega}})^2 + (\gamma_{10}\overline{\delta\sqrt{\omega}})^2 - 4\sqrt{2}\zeta_9(\overline{\delta\sqrt{\omega}})^2 + 2\sqrt{2}\gamma_{10}\gamma_{11}(\overline{\delta\sqrt{\omega}})^2. \quad (37)$$

The substitution of Eq. (36) into (37) yields

$$4\sqrt{2}\zeta_9 = \kappa^2\left(\gamma_5^2 + \gamma_4^2 - 2\sqrt{2}\gamma_4\gamma_5 + \frac{1}{2}\left[\hat{I}'\left(\frac{9\pi}{4}\right)\right]^2 (l_A - l_B)^2 \frac{D^{1/2}}{r^2}\right), \quad (38)$$

which leads to $\kappa^2\zeta_3 = \zeta_9$ with the help of Eq. (34). Therefore, we have proved our conjecture: the scaling factor κ enters quadratically in the relationship between the coefficients of the second-order term of the Taylor expansion of the traces.

Fig. 8 shows the scaling of traces at $\xi_A = \pi$, where a 3-point periodic orbit takes place. The scaling properties for this part of the spectrum can be studied by expanding to the first order the functions under investigation at $\xi_A = \pi$, which yields:

$$x_i \approx \pm 2 \mp 2\eta_i \frac{D^{1/4} l_A}{r} \delta\sqrt{\omega}, \quad (39)$$

where $\eta_i = ((n_i^{(A)})^2 + C(n_i^{(B)})^2)$. In addition, according to recursive rules of the elementary cell, the limits of $n_{i+3}^{(A)}/n_i^{(A)}$ and $n_{i+3}^{(B)}/n_i^{(B)}$ for $i \to \infty$ are

$$\lim_{i\to\infty}\frac{n_{i+3}^{(A)}}{n_i^{(A)}} = \lim_{i\to\infty}\frac{n_{i+3}^{(B)}}{n_i^{(B)}} = \phi^3, \quad (40)$$

where ϕ is the golden ratio, and $\lim_{i\to\infty} n_i^{(A)}/n_i^{(B)} = \phi$. Then, Eqs. (39) and (40) lead to the approximation $\eta_{i+3} \approx \phi^6\eta_i$. This explains the fact that the scaling factor for 3-periodic periodic orbits at increasing index i is $\kappa = \phi^6 = 17.944$, as highlighted in Fig. 8. We have focused in the figure on the behaviour of the functions about the value of 2,
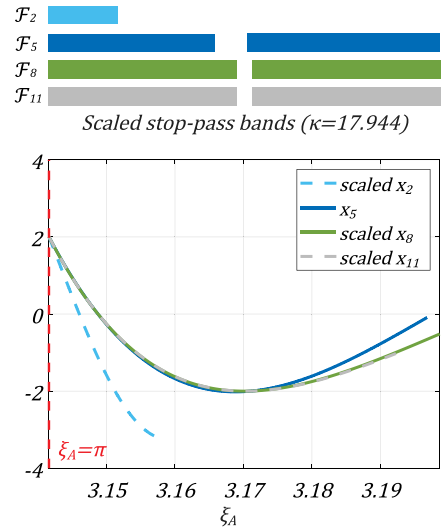

Fig. 8. Canonical multi-supported beam with $C = 5$ (see Fig. 4). Plot of traces $x_2(\sqrt{\omega}/\kappa)$, $x_5(\sqrt{\omega})$ (not scaled), $x_8(\sqrt{\omega}\kappa)$ and $x_{11}(\sqrt{\omega}\kappa^2)$ in the neighbourhood of frequency $\xi_A = \pi$ ($\kappa = 17.944$) at a 3-point periodic orbit occurs.

however the plots show that the same scaling factor describes well the curvatures of traces and then the scaling of stop and pass bands in the neighbourhood of $\xi_A = \pi$, as depicted on the top part of the figure. With a similar procedure, the scaling factor $\kappa = \phi^2 = 2.618$ at the 'fixed point' ($\xi_A = 2\pi$ in both Figs. 4 and 5) can be determined.

By observing the trends in the last three figures, the scaling effect becomes more and more accurate with the increasing of index i. A way to analyse this feature is to specialise Eq. (30) to the case where the p-periodic orbit is followed q times; it turns out that

$$\delta\hat{\mathbf{r}}_{i+pq} \approx C^+(\kappa^+)^q\psi^+ \approx (\kappa^+)^q\delta\mathbf{r}_i. \quad (41)$$

With q increasing, the direction of vector $\delta\hat{\mathbf{r}}_{i+pq}$ is better and better approximated to the direction of ψ^+ because the dominance of the eigenvalue κ^+.

5. Conclusions

Periodic quasicrystalline-based phononic waveguides generated by the Fibonacci sequence can be investigated as a collection of elementary cells whose dispersion spectra are linked by a function, the Kohmoto's invariant, that is an invariant of the set and depends only on the wave frequency. The manifestation of this close connection is the self-similarity of the layout of stop and pass bands in the neighbourhood of specific frequencies.

This paper aims at extending the notion of *canonical configuration* defined for axial waves in bars to periodic multi-supported flexural waveguides whose elementary cells are provided by the standard Fibonacci sequence. The outcomes can be summarised as follows:

(i) the dispersive properties of one of the waveguides under investigation are entirely determined by the behaviour of the trace of the transmission matrix as a function of circular frequency. For any given frequency, the traces corresponding to three arbitrary subsequent cells are related through a recursive relationship which allows us to represent them geometrically as coordinates of points which describe an orbit on the surface defined by the Kohmoto's invariant;

(ii) unlike the companion problem of propagation of axial waves in bars, canonical configurations for homogeneous multi-supported beams can be defined with reference to a specific rational value of the ratio between the distances of the supports. Due to the presence of hyperbolic functions in the dispersion relation, these structures display *almost periodic* frequency spectra for canonical configurations. We proved that

departure from perfect periodicity is relatively small for frequencies for which $\xi_A > \pi$, therefore the theory of canonical structures can be also applied in the current context;

(iii) a self-similar layout of the stop-/pass-band diagram is observed for *canonical* multi-supported beams. Analytical factor governing the scaling of the self similarity are derived through the linearisation of the trace map concerning the relevant periodic orbits. Depending on the number of points p composing the orbits, portions of spectra corresponding to elementary cells for the order i, $i + p/2$ and $i + p$ are related by employing these factors. A detailed analysis of the frequency ranges where the scaling is effective is performed.

The current investigation is preliminary to the analysis of propagation of flexural waves in free quasi-crystalline generated beams that is an open problem in phononic meta-structures.

CRediT authorship contribution statement

Zhijiang Chen: Writing – original draft, Investigation. **Massimiliano Gei:** Writing – original draft, Supervision. **Lorenzo Morini:** Writing – original draft, Supervision.

Declaration of competing interest

The authors declare that they have no known competing financial interests or personal relationships that could have appeared to influence the work reported in this paper.

Data availability

No data was used for the research described in the article.

Acknowledgments

References

Bacigalupo, A., De Bellis, M.L., Vasta, M., 2022. Design of tunable hierarchical waveguides based on Fibonacci-like microstructure. Int. J. Mech. Sci. 224, 107280.

Beli, D., Rosa, M.I.N., De Marqui, C., Ruzzene, M., 2022. Wave beaming and diffraction in quasicrystalline elastic metamaterial plates. Phys. Rev. Res. 4, 043030.

Brun, M., Guenneau, S., Movchan, A.B., 2009. Achieving control of in-plane elastic waves. Appl. Phys. Lett. 94, 061903.

Chen, Y., Kadic, M., Guenneau, S., Wegener, M., 2020. Isotropic chiral acoustic phonons in 3D quasicrystalline metamaterials. Phys. Rev. Lett. 124, 235502.

Chen, Z., Morini, L., Gei, M., 2022. On the adoption of canonical quasi-crystalline laminates to achieve pure negative refraction of elastic waves. Proc. R. Soc. A 380, 20210401.

Chen, Z., Morini, L., Gei, M., 2023. Negative refraction for anti-plane elastic waves in canonical quasicrystalline laminates. Eur. J. Mech. A. Solids 100, 104577.

Davies, B., Chaplain, G.J., Starkey, T.A., Craster, R.V., 2023. Graded quasiperiodic metamaterials perform fractal rainbow trapping. Phys. Rev. Lett. 131, 177001.

Davies, B., Craster, R.V., 2022. Symmetry-induced quasicrystalline waveguides. Wave Motion 115, 103068.

Farhat, A.K.M., Morini, L., Gei, M., 2022. Silver-mean canonical quasicrystalline-generated phononic waveguides. J. Sound Vib. 523, 116679.

Gei, M., 2010. Wave propagation in quasiperiodic structures, stop/pass band distribution and prestress effects. Int. J. Solids Struct. 47, 3067–3075.

Gei, M., Chen, Z., Bosi, F., Morini, L., 2020. Phononic canonical quasicrystalline waveguides. Appl. Phys. Lett. 116, 241903.

Kohmoto, M., Oono, Y., 1984. Cantor spectrum for an almost periodic schroedinger equation and a dynamical map. Phys. Lett. 102A, 145–148.

Kolar, M., Ali, M.K., 1989. Generalized fibonacci superlattices, dynamical trace maps, and magnetic excitations. Phys. Rev. B 39, 426–432.

Ma, J., Zhou, D., Sun, K., Mao, X., Gonella, S., 2018. Edge modes and asymmetric wave transport in topological lattices: experimental characterization at finite frequencies. Phys. Rev. Lett. 121, 094301.

Morini, L., Eyzat, Y., Gei, M., 2019a. Negative refraction in quasicrystalline multilayered metamaterials. J. Mech. Phys. Solids 124, 282–298.

Morini, L., Gei, M., 2018. Waves in one-dimensional quasicrystalline structures: dynamical trace mapping, scaling and self-similarity of the spectrum. J. Mech. Phys. Solids 119, 83–103.

Morini, L., Tetik, Z.G., Shmuel, G., Gei, M., 2019b. On the universality of the frequency spectrum and band-gap optimization of quasicrystalline-generated structure rods. Phil. Trans. R. Soc. A 378, 20190240.

Morvan, B., Tinel, B., Hladky-Hennion, A.C., Vasseur, J., Dubus, B., 2010. Experimental demonstration of the negative refraction of a transverse elastic wave in a two-dimensional solid phononic crystal. Appl. Phys. Lett. 96, 101905.

Norris, A.N., 2008. Acoustic cloaking theory. Proc. R. Soc. A 464, 2411–2434.

Pal, R.K., Rosa, M.I.N., Ruzzene, M., 2019. Topological bands and localized vibration modes in quasiperiodic beams. New J. Phys. 21, 093017.

Poddubny, A.N., Ivchenko, E.L., 2010. Photonic quasicrystalline and aperiodic structures. Physica E 43, 1871–1895.

Rosa, M.I.N., Pal, R.K., Arruda, J.R.F., Ruzzene, M., 2019. Edge states and topological pumping in spatially modulated elastic lattices. Phys. Rev. Lett. 123, 034301.

Shmuel, G., Band, R., 2016. Universality of the frequency spectrum of laminates. J. Mech. Phys. Solids 92, 127–136.

Sorokin, V.S., 2019. Longitudinal wave propagation in a one-dimensional quasi-periodic waveguide. Proc. R. Soc. A 475, 20190392.

Srivastava, A., 2016. Metamaterial properties of periodic laminates. J. Mech. Phys. Solids 96, 252–263.

Tol, S., Degertekin, F.L., Erturk, A., 2017. Structurally embedded reflectors and mirrors for elastic wave focusing and energy harvesting. J. Appl. Phys. 122, 164503.

Wang, P., Lu, L., Bertoldi, K., 2015. Topological phononic crystals with one-way elastic edge waves. Phys. Rev. Lett. 115, 104302.

Xia, Y., Erturk, A., Ruzzene, M., 2020. Topological edge states in quasiperiodic locally resonant metastructures. Phys. Rev. Appl. 13, 014023.

Yang, S., Page, J.H., Liu, Z., Cowan, M.L., Chan, C.T., Sheng, P., 2004. Focusing of sound in a 3D phononic crystal. Phys. Rev. Lett. 93, 024301.

Zhang, H.F., 2017. Investigations on the two-dimensional aperiodic plasma photonic crystals with fractal fibonacci sequence. AIP Adv. 7, 075102.

Zhang, X., Liu, Z., 2004. Negative refraction of acoustic waves in two-dimensional phononic crystals. Appl. Phys. Lett. 85, 341–342.